

Leveraging Large-Scale Pretrained Spatial-Spectral Priors for General Zero-Shot Pansharpening

Yongchuan Cui^{1,2}, Peng Liu^{1,2,*}, Yi Zeng³

¹Aerospace Information Research Institute, Chinese Academy of Sciences

²School of Electronic, Electrical and Communication Engineering, University of Chinese Academy of Sciences

³College of Information, Beijing Forestry University

yongchuancui@gmail.com, liupeng202303@aircas.ac.cn, zengyi@bjfu.edu.cn

Abstract

Existing deep learning methods for remote sensing image fusion often suffer from poor generalization when applied to unseen datasets due to the limited availability of real training data and the domain gap between different satellite sensors. To address this challenge, we explore the potential of foundation models by proposing a novel pretraining strategy that leverages large-scale simulated datasets to learn robust spatial-spectral priors. Specifically, our approach first constructs diverse simulated datasets by applying various degradation operations (blur, noise, downsampling) and augmentations (bands generation, channel shuffling, high-pass filtering, color jittering, etc.) to natural images from ImageNet and remote sensing images from SkyScript. We then pre-train fusion models on these simulated data to learn generalizable spatial-spectral representations. The pretrained models are subsequently evaluated on six datasets (WorldView-2/3/4, IKONOS, QuickBird, GaoFen-2) using zero-shot and one-shot paradigms, with both full- and freeze-tuning approaches for fine-tuning. Extensive experiments on different network architectures including convolutional neural networks, Transformer, and Mamba demonstrate that our pretraining strategy significantly improves generalization performance across different satellite sensors and imaging conditions for various fusion models. The pretrained models achieve superior results in zero-shot scenarios and show remarkable adaptation capability with minimal real data in one-shot settings. Our work provides a practical solution for cross-domain pansharpening, establishes a new benchmark for generalization in remote sensing image fusion tasks, and paves the way for leveraging foundation models through advanced training strategies.

Introduction

Remote sensing image fusion plays a crucial role in Earth observation by combining complementary information from multiple sources to create comprehensive and high-quality imagery. Among various fusion techniques, pansharpening has emerged as a fundamental task that aims to enhance the spatial resolution of multispectral images (MS) by integrating high-resolution panchromatic imagery (PAN) while preserving spectral characteristics.

The evolution from traditional fusion methods to deep learning-based approaches has marked a significant advancement in the field (Vivone et al. 2021; Liu et al. 2022).

*Corresponding author.

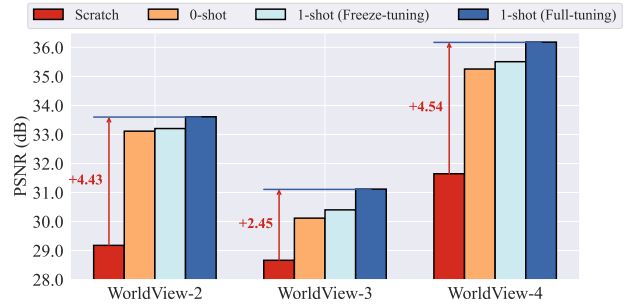


Figure 1: Comparison of PEMA (Cui et al. 2024a) model w/ and w/o pretraining on SkyScript (Wang et al. 2024b).

While classical techniques such as component substitution and multiresolution analysis have provided reasonable results, they often struggle with spectral distortion and spatial artifacts (Vivone et al. 2021; Meng et al. 2021). In recent years, deep learning methods have demonstrated remarkable improvements in both spatial and spectral fidelity, achieving superior performance compared to traditional approaches through their ability to learn complex spatial-spectral relationships (Liu et al. 2022; Deng et al. 2022).

Despite the substantial progress made by deep learning models, they suffer from significant generalization challenges when applied to unseen datasets or different satellite sensors. The domain gap between training and testing scenarios, limited availability of real training data, and variations in imaging conditions across different sensors pose substantial obstacles to robust performance (Wang et al. 2024a; Dian, Guo, and Li 2023; Xing et al. 2025; Sun et al. 2026). Large-scale foundation models have shown exceptional generalization capabilities in various computer vision tasks through their massive parameter sizes and extensive training data, effectively spanning vast sample spaces. Nevertheless, in the pansharpening domain, the lack of large-scale training datasets has hindered the development and adoption of foundation models, preventing the field from benefiting from their superior generalization properties. The most convincing evidence is that there still hasn't emerged any large-scale foundation model with massive parameters specifically designed for pansharpening tasks.

Therefore, rather than focusing on model architecture design, this work emphasizes dataset synthesis and pre-training strategies for pansharpening models. Our primary objective is to explore large-scale pretraining approaches specifically tailored for pansharpening tasks. We propose learning spatial-spectral priors from large-scale simulated datasets and conduct extensive experiments across diverse network architectures including convolutional neural networks (CNNs) (Krizhevsky, Sutskever, and Hinton 2017), Transformers (Dosovitskiy et al. 2021), and Mamba (Gu and Dao 2023), demonstrating that large-scale simulated pre-training significantly enhances model generalization capabilities. To rigorously evaluate the model’s generalization and adaptation to real datasets, we conducted challenging zero-shot (pretraining only) and one-shot (fine-tuning on one single image) experiments. As shown in Fig. 1, the results on WorldView-2/3/4 (Meng et al. 2021) datasets demonstrate that pretraining achieves significantly better performance compared to training from scratch, and full fine-tuning (updating all parameters) outperforms freeze fine-tuning (only updating the final convolutional layer). The results show promising performance in both zero-shot and one-shot learning scenarios, establishing a practical foundation for cross-domain pansharpening applications and the development of foundation models for pansharpening. To the best of our knowledge, this is the first work to explore the potential of large-scale pretraining for pansharpening tasks.

Related Work and Motivation

Deep Learning Methods for Pan-sharpening

Traditional pansharpening methods, including component substitution (Laben and Brower 2000; Shah, Younan, and King 2008; Rahmani et al. 2010), multi-resolution analysis (Aiazzi et al. 2002, 2006), and variational optimization (Vivone et al. 2015; Wu et al. 2022) approaches, have been extensively studied but face limitations in spectral-spatial fidelity and computational efficiency (Vivone et al. 2021; Meng et al. 2021). The landscape of pansharpening underwent a paradigm shift with the introduction of deep learning methodologies, fundamentally transforming the approach from handcrafted feature engineering to data-driven representation learning (Liu et al. 2022; Deng et al. 2022; Liu et al. 2024).

Pioneering convolutional architectures demonstrated unprecedented capabilities in capturing complex spatial-spectral correlations. Models like PNN (Masi et al. 2016), PanNet (Yang et al. 2017) and MSDCNN (Yuan et al. 2018) established the foundation for learning-based fusion strategies, proving that neural networks could effectively approximate the intricate spectral mapping by hierarchical feature extraction. Since then, various deep learning models spring up. For instance, the introduction of Transformer architectures (Vaswani et al. 2017; Dosovitskiy et al. 2021) marked a significant milestone, offering the capability to model long-range dependencies through self-attention mechanisms. Specialized Transformer variants for pansharpening (Meng et al. 2022; Deng et al. 2023; Cui et al. 2024a; Bandara and Patel 2022; Jiang and Chen

2025) have demonstrated remarkable performance improvements. To address the quadratic computational complexity of Transformers, various Mamba (Gu and Dao 2023; Dao and Gu 2024) models that combine structured state space sequence models with dynamic selective mechanisms for more efficient computation have emerged, such as Pan-Mamba (He et al. 2025), FusionMamba (Peng et al. 2024) and S²CMamba (Zhang et al. 2025). Generative modeling approaches also emerged as a promising direction for enhancing the fidelity of fused outputs. Generative adversarial networks (Cui et al. 2024b; Ma et al. 2020; Liu et al. 2020, 2023) and diffusion-based methods (Cao et al. 2024; Zhong et al. 2024; Meng et al. 2023; Rui et al. 2024; Xing et al. 2024a,b) have shown particular promise in generating more realistic and detailed fused imagery.

Motivation

Despite the efforts, the generalization of deep learning-based pansharpening models in real-world scenarios remains challenging. Methods such as unsupervised learning (Ma et al. 2020; Ciotola, Poggi, and Scarpa 2023; Rui et al. 2024; Cui et al. 2025b) paradigms to remove the need for paired data, generalized module design (Xing et al. 2024a, 2025; Cui, Liu, and Zhang 2025) strategies to enhance robustness have been proposed to address this issue. However, these approaches often require extensive architectural modifications or computationally intensive retraining, which limits their practicality for real-world deployment.

The limitations of current approaches motivate our exploration of large-scale pretraining strategies for pansharpening. While foundation models have demonstrated exceptional generalization capabilities in various computer vision domains through massive parameter spaces and extensive training data, the pansharpening field has not fully leveraged these advantages due to the scarcity of large-scale training datasets. This gap presents an opportunity to develop novel pretraining approaches and appropriate datasets construction methods that can bridge the domain-specific challenges of pansharpening with the generalization benefits of foundation models.

Motivated by the observation that a large volume of simulated data can provide a rich and diverse training environment for learning robust spatial-spectral representations, our work is the first to explore simulated pretraining for learning spectral-spatial priors in pansharpening. By constructing large-scale simulated datasets through various degradation operations and augmentations, we create a training space that captures cross-sensor variations and geographic diversity while providing sufficient data volume for effective pretraining. This approach enables us to explore the potential of foundation models in pansharpening without requiring massive amounts of real training data, and paves the way for developing more generalizable pansharpening models.

Proposed Method

To address the scarcity of real pansharpening training data and enhance the generalization ability of deep models, we construct simulated datasets by applying various degradation operations and augmentations to large-scale images.

To investigate the differences between natural image and remote sensing image pretraining, we employ two distinct data sources: natural images from ImageNet (Deng et al. 2009) and remote sensing images from SkyScript (Wang et al. 2024b). Natural images focus more on spatial details and rich color information, providing high-resolution features, rich texture patterns, diverse semantic content, and extensive visual structures that help models learn generalizable spatial-spectral representations, while remote sensing images from SkyScript (Wang et al. 2024b), a multi-source dataset encompassing diverse satellite sensors including high-resolution commercial satellites (Planet SkySat), multispectral satellites (Landsat 8/9, Sentinel-2), and aerial imagery from various geographical regions, offer domain-specific characteristics, authentic spectral-spatial relationships, and real-world radiometric data that are more closely aligned with real pansharpening scenarios.

Simulated Dataset Construction

Due to the non-uniformity of data channels across different sources, such as ImageNet (Deng et al. 2009) containing only RGB channels and products from different satellites carrying various sensors with different numbers of spectral bands, we first simulate the generation of additional spectral bands, setting the maximum number of bands to C_{\max} .

Multispectral Image Synthesis For a given image $\mathbf{I} \in \mathbb{R}^{C \times H \times W}$ with C channels where H and W represent the height and width of the image in pixels, respectively (e.g., RGB images with $C = 3$ or Landsat-7 ETM+ with $C = 7$ excluding panchromatic band), we generate a simulated higher-dimensional multispectral image $\mathbf{I}_{\text{MS}} \in \mathbb{R}^{C_{\max} \times H \times W}$ by synthesizing additional spectral bands through linear combinations of existing channels:

$$\mathbf{I}_{\text{MS}}^{(C+1:C_{\max})} = \mathbf{A}\mathbf{I}, \quad (1)$$

where $\mathbf{A} = [\alpha_{ij}] \in \mathbb{R}^{(C_{\max}-C) \times C}$ is a randomly generated weight matrix with each row normalized to sum to unity:

$$\alpha_{ij} = \frac{\tilde{\alpha}_{ij}}{\sum_{k=1}^C \tilde{\alpha}_{ik}}, \quad \tilde{\alpha}_{ij} \sim \text{Uniform}(0, 1). \quad (2)$$

For a specific band in the synthesized multispectral image, we have:

$$\mathbf{I}_{\text{MS}}^{(i)} = \sum_{j=1}^C \alpha_{ij} \mathbf{I}^{(j)}, \quad i = C+1, C+2, \dots, C_{\max}, \quad (3)$$

where $\mathbf{I}^{(j)}$ represents the j -th channel of the original image and $\mathbf{I}_{\text{MS}}^{(i)}$ represents the i -th channel of the synthesized multispectral image.

Simulated PAN Image Generation Given a multispectral image $\mathbf{I}_{\text{MS}} \in \mathbb{R}^{C \times H \times W}$ with C spectral bands, similar to the multispectral image synthesis, we simulate a panchromatic image $\mathbf{I}_{\text{PAN}} \in \mathbb{R}^{1 \times H \times W}$ through a weighted linear combination of a random subset of spectral bands:

$$\mathbf{I}_{\text{PAN}} = \sum_{i \in \mathcal{S}} w_i \mathbf{I}_{\text{MS}}^{(i)}, \quad (4)$$

where $\mathcal{S} \subset \{1, 2, \dots, C\}$ is a randomly selected subset of spectral bands with $|\mathcal{S}| \in [2, C]$, $|\cdot|$ denotes the cardinality of a set, and $\mathbf{w} = [w_1, w_2, \dots, w_{|\mathcal{S}|}]$ are randomly generated weights that sum to unity:

$$w_i = \frac{\tilde{w}_i}{\sum_{j \in \mathcal{S}} \tilde{w}_j}, \quad \tilde{w}_i \sim \text{Uniform}(0, 1). \quad (5)$$

Eq. (5) mimics the physical process where panchromatic sensors capture a weighted combination of multiple spectral bands, with the weights varying depending on the sensor's randomly generated spectral response characteristics.

Training Strategy

Contemporary supervised pansharpening methods predominantly adopt Wald's protocol (Wald, Ranchin, and Mangolini 1997) for degradation-reconstruction proxy learning, where multispectral and panchromatic images undergo fixed-ratio downsampling and blurring (simulating modulation transfer function and point spread function characteristics) to establish low-to-high spectral mapping, with original MS as ground truth (GT) signal. While effective for learning spectral-spatial correspondences, this rigid degradation pipeline severely limits generalization capability. Networks risk memorizing sensor-specific deblurring/upsampling patterns rather than learning transferable restoration principles. To address this, we design various stochastic degradation and augmentation operations. This forces the network to learn generalized representations of cross-resolution spectral fidelity and spatial detail injection, rather than overfitting to deterministic degradation patterns.

Given a clean multispectral image $\mathbf{I}_{\text{MS}} \in \mathbb{R}^{C_{\max} \times H \times W}$ and a clean panchromatic image $\mathbf{I}_{\text{PAN}} \in \mathbb{R}^{1 \times H \times W}$, we generate degraded inputs via a composite transformation:

$$(\mathbf{I}_{\text{MS}}^{\text{deg}}, \mathbf{I}_{\text{PAN}}^{\text{deg}}) = \mathcal{D} \circ \mathcal{A}(\mathbf{I}_{\text{MS}}, \mathbf{I}_{\text{PAN}}), \quad (6)$$

where \mathcal{A} denotes the augmentation operator, \mathcal{D} denotes the degradation operator, and \circ represents function composition.

Degradation Operator \mathcal{D} The degradation operator is defined as a composition:

$$\mathcal{D} = \mathcal{B}_{\xi} \circ \mathcal{D}_s \circ \mathcal{N}_{\psi}, \quad (7)$$

where \mathcal{B}_{ξ} is a blur operator with kernel ξ , \mathcal{D}_s is a downsampling operator with scale factor s , and \mathcal{N}_{ψ} is a noise operator parameterized by type ψ .

(1) Blur Operator \mathcal{B}_{ξ} :

$$\mathbf{I}^{\text{blur}} = \mathcal{B}_{\xi}(\mathbf{I}) = \mathcal{K}_{\xi} * \mathbf{I}, \quad (8)$$

where $*$ denotes convolution, \mathcal{K}_{ξ} is randomly chosen from:

$$\mathcal{K}_{\xi} \in \{\mathcal{G}_{\sigma,k}, \mathcal{B}_k, \mathcal{M}_{\theta,d,k}, \mathcal{M}_k\}, \quad (9)$$

with Gaussian $\mathcal{G}_{\sigma,k}$, Box \mathcal{B}_k , Motion $\mathcal{M}_{\theta,d,k}$, and Median \mathcal{M}_k blur kernels, and uniformly sampled parameters:

$$\sigma \in [0.1, 3.0], \quad \theta \in [0^\circ, 360^\circ], \quad d \in [-1, 1], \quad k \in \{3, 5, 7\}.$$

(2) Downsampling Operator \mathcal{D}_s :

$$\mathbf{I}^{\text{down}} = \mathcal{D}_s(\mathbf{I}), \quad s \in [0.1, 0.5], \quad (10)$$

where s represents the down scale factor (we set $2\times$ to $10\times$ downsampling to simulate multi-scale degradation scenarios), and \mathcal{D}_s uses a random interpolation method from:

$$\{\text{Nearest, Bilinear, Bicubic, Area}\}.$$

(3) Noise Operator \mathcal{N}_ψ :

$$\mathbf{I}^{\text{noisy}} = \mathbf{I} + \mathcal{N}_\psi(\mathbf{I}), \quad (11)$$

with $\mathcal{N}_\psi \in \{\mathcal{N}_G, \mathcal{N}_{SP}, \mathcal{N}_P, \mathcal{N}_S\}$ is a random noise operator:

$$\begin{aligned} \mathcal{N}_G(\mathbf{I}) &= \mathcal{N}(0, \sigma^2), & \sigma &\in [0.01, 0.1] \quad (\text{Gaussian}) \\ \mathcal{N}_{SP}(\mathbf{I}) &= \mathcal{S}(p), & p &\in [0.001, 0.01] \quad (\text{Salt \& Pepper}) \\ \mathcal{N}_P(\mathbf{I}) &= \frac{\mathcal{P}(\lambda \mathbf{I})}{\lambda}, & \lambda &\in [10, 50] \quad (\text{Poisson}) \\ \mathcal{N}_S(\mathbf{I}) &= \mathbf{I} \odot \mathcal{N}(1, \sigma^2), & \sigma &\in [0.05, 0.2] \quad (\text{Speckle}) \end{aligned}$$

where \odot denotes element-wise multiplication.

Augmentation Operator \mathcal{A} The augmentation operator \mathcal{A} is composed of:

$$\mathcal{A} = \mathcal{A}_{\text{spatial}} \circ \mathcal{A}_{\text{spectral}}, \quad (12)$$

where $\mathcal{A}_{\text{spatial}}$ includes geometric transformations, and $\mathcal{A}_{\text{spectral}}$ applies spectral perturbations.

(1) Spatial Augmentations $\mathcal{A}_{\text{spatial}}$:

$$\mathcal{A}_{\text{spatial}} \in \{\text{Flip}_{x,y}, \text{Rotate}_{k \cdot 90^\circ}\}, \quad k \in \{0, 1, 2, 3\}, \quad (13)$$

for horizontal and vertical flips, and discrete rotations.

(2) Spectral Augmentations $\mathcal{A}_{\text{spectral}}$ includes:

- *Channel Shuffle*:

$$\mathbf{I}^{\text{aug}} = \mathbf{I}[\pi], \quad \pi \sim \text{Permutation}(\{1, \dots, C_{\text{max}}\}). \quad (14)$$

- *Channel Masking*:

$$\mathbf{I}_i^{\text{aug}} = \begin{cases} 0, & i \in \mathcal{M}, \\ \mathbf{I}_i, & \text{otherwise}, \end{cases} \quad \mathcal{M} \subset \{1, \dots, C_{\text{max}}\}. \quad (15)$$

- *High-Pass Filtering (PAN only)*:

$$\mathbf{I}^{\text{aug}} = \mathcal{H}_\zeta * \mathbf{I}, \quad \mathcal{H}_\zeta \in \{\mathcal{L}_3, \mathcal{G}_{0.5,3} - \mathcal{G}_{2.0,7}, \mathcal{S}, \mathcal{C}\}, \quad (16)$$

where \mathcal{L}_3 is Laplacian filter with kernel size of 3, and the DoG filter ($\mathcal{G}_{0.5,3} - \mathcal{G}_{2.0,7}$) uses $\sigma = 0.5/2.0$ and kernel sizes 3/7. \mathcal{S} and \mathcal{C} are Sobel and Canny filters.

- *Color Jittering*:

$$\mathcal{T}_{\text{color}} = \mathcal{T}_{\text{bri}} \circ \mathcal{T}_{\text{con}} \circ \mathcal{T}_{\text{sat}} \circ \mathcal{T}_{\text{hue}}, \quad (17)$$

applied sequentially to simulate radiometric changes, where $\mathcal{T}_{\text{color}}$ represents the color transformation function composed of brightness $\mathcal{T}_{\text{brightness}}$, contrast $\mathcal{T}_{\text{contrast}}$, saturation $\mathcal{T}_{\text{saturation}}$, and hue \mathcal{T}_{hue} transformations.

Loss Function During pretraining and fine-tuning, we employ \mathcal{L}_1 loss to measure the pixel-wise difference between the predicted image and the ground truth:

$$\mathcal{L}_1 = \frac{1}{C_{\text{max}} \times H \times W} \sum_{c,h,w} |\mathbf{I}_{\text{MS}}^{(c,h,w)} - \mathcal{F}(\mathbf{I}_{\text{MS}}^{\text{deg}}, \mathbf{I}_{\text{PAN}}^{\text{deg}})^{(c,h,w)}|, \quad (18)$$

where \mathbf{I}_{MS} represents the original high-resolution multi-spectral image (HRMS) as ground truth, $\mathbf{I}_{\text{MS}}^{\text{deg}}$ and $\mathbf{I}_{\text{PAN}}^{\text{deg}}$ denote the degraded low-resolution multispectral (LRMS) and panchromatic images as network inputs, $\mathcal{F}(\cdot, \cdot)$ represents the fusion network that takes both degraded images as input, and C_{max} is the maximum number of spectral bands. To handle varying numbers of bands, the network will use fixed C_{max} channels of input and output. Zero-padding is applied to input images in case of bands less than C_{max} .

Zero-shot Generalization and One-shot Tuning

To evaluate the generalization and adaptation capabilities of pretrained pansharpening models, we consider two practical settings: *zero-shot generalization* and *one-shot tuning*.

In the zero-shot setting, the pretrained model \mathcal{F}_{pre} is directly applied to unseen satellite datasets without any fine-tuning:

$$\hat{\mathbf{I}}_{\text{MS}} = \mathcal{F}_{\text{pre}}(\mathbf{I}_{\text{MS}}^{\text{deg}}, \mathbf{I}_{\text{PAN}}^{\text{deg}}), \quad (19)$$

where $\mathbf{I}_{\text{MS}}^{\text{deg}}$ and $\mathbf{I}_{\text{PAN}}^{\text{deg}}$ are the degraded inputs using the widely used Wald's protocol (Wald, Ranchin, and Mangolini 1997) and $\hat{\mathbf{I}}_{\text{MS}}$ is the predicted fused image.

In the one-shot setting, we fine-tune the pretrained model using only a single pair of degraded inputs. Two strategies are considered:

(1) *Full-tuning*: All model parameters are updated to minimize the \mathcal{L}_1 loss:

$$\mathcal{L}_{\text{full}} = \mathcal{L}_1(\mathcal{F}_{\text{full}}(\mathbf{I}_{\text{MS}}^{\text{deg}}, \mathbf{I}_{\text{PAN}}^{\text{deg}}), \mathbf{I}_{\text{MS}}). \quad (20)$$

(2) *Freeze-tuning*: Only the final output layer is updated while keeping all backbone parameters frozen:

$$\mathcal{L}_{\text{freeze}} = \mathcal{L}_1(\mathcal{F}_{\text{freeze}}(\mathbf{I}_{\text{MS}}^{\text{deg}}, \mathbf{I}_{\text{PAN}}^{\text{deg}}), \mathbf{I}_{\text{MS}}). \quad (21)$$

This lightweight adaptation enables robust cross-domain performance with minimal tuning data. Especially, the challenging one-shot tuning uses only a single pair of inputs.

Experiments

Setups

In our experiments, we conduct pretraining on several representative pansharpening models with different architectures, including CNN: FusionNet (Deng et al. 2021), GPPNN (Xu et al. 2021), PreMix (Cui et al. 2025a), Transformer: PE-MAE (Cui et al. 2024a), and Mamba: PanMamba (He et al. 2025), using both the ImageNet (Deng et al. 2009) and SkyScript (Wang et al. 2024b) datasets. For each satellite dataset, we conduct one-shot experiments using only 10 images (the rest are for validating) and report the results with model checkpoint of best PSNR on validation set. The details of datasets, evaluation metrics, and implementations are provided in the Appendix.

Results

Model / Dataset	ImageNet	SkyScript
4×	FusionNet	38.08/0.9682
	GPPNN	38.61/0.9696
	PreMix	39.22/0.9701
	PEMAE	40.95/0.9726
	PanMamba	46.87/0.9861
8×	FusionNet	33.55/0.9539
	GPPNN	34.56/0.9588
	PreMix	35.41/0.9612
	PEMAE	37.71/0.9666
	PanMamba	42.39/0.9838

Table 1: Reconstruction performance (PSNR/SSIM) under 4× and 8× spatial resolution degradations.

Model	#Params			MACs (G)
	Total (K)	Tunable (K)	Ratio (%)	
FusionNet	78.63	2.31	2.94	5.13
GPPNN	238.59	10.24	4.29	15.64
PreMix	616.11	41.62	6.75	40.34
PEMAE	388.18	2.31	0.60	20.42
PanMamba	497.14	2.31	0.47	14.33

Table 2: Comparison of model parameter counts (K) and Multiply-Accumulate Operations (MACs, G).

Pretraining Results Table 1 summarizes the performance of different pansharpening models pretrained on simulated datasets derived from ImageNet and SkyScript under 4× and 8× spatial resolution degradations. Across all architectures, pretraining on SkyScript consistently yields higher PSNR and SSIM scores compared to ImageNet. Among the models, PEMAe achieves the best performance on both datasets and at both degradation levels, demonstrating the advantage of Transformer-based architectures in capturing long-range dependencies and complex spectral relationships. PanMamba achieves the second-best performance, followed by CNN-based models. Notably, the performance gap between 4× and 8× settings highlights the increased challenge of higher degradation, but the relative ranking of models remains consistent, underscoring the robustness of the pretraining strategy. For visualization of predicted results, please refer to Appendix.

Reduced-Resolution Evaluation Table 3 presents a comprehensive quantitative comparison of different models and training strategies. Several key observations emerge: (1) Models trained from scratch (index ¹) generally underperform compared to those utilizing pretraining, especially in cross-domain (0-shot) and adaptation (1-shot) scenarios. 0-shot generalization (indices ² and ³) already provides a significant boost over training from scratch, demonstrating the transferability of the learned spatial-spectral priors. (2) One-shot full-tuning (indices ⁶ and ⁷) achieves the

best results for most models and datasets, indicating that full parameter adaptation enables rapid and effective domain adaptation. (3) Freeze-tuning (indices ⁴ and ⁵) also improves performance but is generally less effective than full-tuning, suggesting that updating all parameters is beneficial for adapting to new domains. This observation differs from high-level vision tasks like classification, where fine-tuning only the classification head often suffices for good performance, highlighting the unique challenges of low-level vision tasks that require pixel-level precision and spatial-spectral alignment. (4) Interestingly, while PEMAe achieves the best performance during pretraining (as shown in Table 1), CNN-based models demonstrate superior performance in 0-shot generalization scenarios (indices ² and ³). While Transformer-based models excel at learning complex long-range dependencies during pretraining, CNN architectures provide better generalization capabilities for unseen real satellite datasets. This can be attributed to the capabilities in capturing local spatial patterns and inductive bias towards spatial locality, making them more robust when transferring from simulated to real satellite data with varying spectral characteristics.

According to Table 2, the performance differences may be related to both total parameter count and the ratio of tunable parameters during fine-tuning. PreMix, with the highest tunable parameter ratio (6.75%) and largest model size (616.11K parameters), achieves the best performance, suggesting that having more adaptable parameters benefits domain adaptation. Conversely, PEMAe and PanMamba, despite having very low tunable ratios (0.60% and 0.47%, respectively), still achieve competitive performance, indicating that the quality of pretrained representations and architectural design can compensate for limited parameter adaptation. These results collectively demonstrate that the proposed pretraining strategy, especially when combined with minimal fine-tuning, substantially enhances the generalization and adaptation capabilities of pansharpening models.

Full-Resolution Evaluation Table 3 also reports the full-resolution evaluation results. The trends observed in reduced-resolution evaluation persist: models with pretraining and subsequent full-tuning (indices ⁶ and ⁷) achieve the best or near-best results across most datasets and models. The results confirm that large-scale simulated pretraining, followed by targeted adaptation, enables models to generalize well to real satellite data and maintain high-quality fusion outputs in challenging full-resolution scenarios.

Notably, GPPNN achieve the best QNR and lowest distortion metrics in most cases, training from scratch. This demonstrates that improving model generalization through meticulous architectural design remains a viable approach, but requires extensive domain-specific engineering. According to Table 3, our pretraining approach is universally applicable to most models, providing consistent performance improvements across different architectures while requiring minimal real data for adaptation.

Visualization Fig. 2 provides visualization comparison, corroborating the quantitative findings: full-tuning enables the model to rapidly adapt to new spectral mappings while

Model	WorldView-2	WorldView-3	WorldView-4	IKONOS	QuickBird	GaoFen-2	
Reduced-Resolution : PSNR↑ / SAM $\times 10^{-2}$ ↓ / ERGAS↓	FusionNet	¹ 30.42/11.1/7.14	31.01/11.05/5.45	34.89/4.09/2.37	35.58/6.37/2.62	40.89/3.11/1.46	38.85/2.82/1.39
		² 32.56/9.62/5.83	29.80/12.09/6.58	35.09/4.11/2.58	35.81/5.24/2.49	39.11/3.11/1.99	34.26/2.96/2.53
		³ 32.45/9.52/5.83	30.07/12.11/6.24	34.72/4.33/2.62	35.82/5.32/2.44	39.21/3.18/1.94	34.00/3.15/2.58
		⁴ 32.86/9.26/5.56	30.09/11.82/6.28	35.44/3.91/2.41	36.19/4.95/2.39	39.95/2.97/1.80	35.26/2.84/2.26
		⁵ 32.63/9.32/5.72	30.27/11.86/6.06	35.00/4.19/2.50	36.12/5.15/2.36	39.80/3.07/1.80	34.69/3.06/2.39
		⁶ 33.58/8.39/4.98	30.94/10.64/5.52	35.97/3.56/2.17	37.08/4.51/2.09	42.52/2.54/1.25	39.50/2.38/1.32
		⁷ 33.56/8.44/4.97	31.07/10.87/5.44	35.96/3.71/2.17	37.10/4.63/2.10	42.68/2.56/1.23	39.18/2.61/1.35
	GPPNN	¹ 30.82/10.2/6.77	30.14/11.62/6.04	34.96/3.60/2.42	34.56/4.99/2.73	40.75/2.78/1.53	39.56/2.31/1.32
		² 33.13/8.95/5.35	29.49/12.46/7.25	34.94/4.14/2.71	35.85/5.11/2.49	39.43/3.00/1.96	34.28/2.91/2.57
		³ 32.94/9.11/5.55	29.61/12.50/7.13	34.03/4.57/3.04	35.87/5.06/2.48	39.28/2.94/1.95	34.09/2.87/2.58
		⁴ 33.54/8.42/5.05	30.35/11.28/6.28	35.77/3.82/2.32	36.40/4.97/2.31	41.19/3.05/1.60	36.55/3.00/1.97
		⁵ 33.44/8.41/5.21	30.42/11.14/6.22	35.35/3.82/2.47	36.72/4.76/2.23	41.50/2.77/1.54	36.41/2.61/1.98
		⁶ 33.78/8.26/4.91	30.70/10.84/5.87	36.16/3.50/2.15	36.87/4.72/2.17	41.56/2.76/1.41	39.48/2.42/1.33
		⁷ 33.89/8.33/4.86	31.01/10.86/5.60	36.18/3.49/2.12	37.07/4.64/2.14	42.64/2.51/1.27	39.52/2.32/1.33
	PreMix	¹ 30.46/9.19/7.18	29.00/14.11/6.75	34.31/3.83/2.59	34.45/5.39/2.75	40.53/2.91/1.55	39.46/2.42/1.33
		² 33.59/8.17/4.92	30.36/10.41/6.10	35.43/3.40/2.36	36.45/4.57/2.26	39.85/2.51/1.75	34.48/2.67/2.33
		³ 32.91/8.72/5.26	29.97/11.08/6.42	34.87/3.57/2.53	36.01/4.94/2.37	39.31/2.76/1.82	34.13/2.58/2.39
		⁴ 33.82/7.88/4.80	30.75/10.17/5.78	35.67/3.39/2.26	36.86/4.33/2.17	40.78/2.38/1.57	35.57/2.70/2.07
		⁵ 33.22/8.51/5.14	30.50/10.75/5.98	35.26/3.60/2.39	36.45/4.64/2.26	40.27/2.61/1.64	35.07/2.59/2.17
		⁶34.24/7.64/4.62	31.60/9.77/5.19	36.25/3.28/2.09	37.57/4.23/1.99	42.69/2.43/1.22	39.70/2.29/1.28
		⁷ 33.90/8.09/4.78	31.34/10.46/5.34	36.21/3.43/2.10	37.10/4.60/2.09	42.45/2.65/1.26	39.44/2.33/1.34
	PEMAE	¹ 29.18/15.7/10.1	28.66/15.87/8.36	31.65/7.22/3.80	34.84/5.86/2.71	40.96/2.98/1.45	37.57/3.19/1.59
		² 33.13/8.38/5.26	30.23/10.90/6.19	35.47/3.69/2.45	36.42/4.72/2.25	39.89/2.77/1.76	34.65/2.81/2.35
		³ 33.11/8.92/5.45	30.12/11.57/6.36	35.25/3.98/2.56	36.23/4.94/2.37	39.99/2.86/1.83	34.65/2.73/2.41
		⁴ 33.25/8.23/5.19	30.43/10.69/6.01	35.70/3.63/2.35	36.68/4.56/2.19	40.40/2.71/1.66	35.22/2.76/2.20
		⁵ 33.20/8.92/5.42	30.40/11.39/6.08	35.51/3.94/2.43	36.60/4.74/2.27	40.67/2.77/1.68	35.34/2.65/2.23
		⁶ 33.71/7.76/4.98	31.21/10.05/5.39	36.31/3.33/2.10	37.52/4.20/1.99	42.95/2.41/1.19	39.58/2.33/1.32
		⁷ 33.61/8.27/5.22	31.12/10.63/5.52	36.18/3.50/2.11	37.52/4.35/2.02	43.21/2.45/1.16	39.71/2.38/1.31
PanMamba	¹ 21.48/36.0/24.1	23.88/25.31/17.4	21.19/23.7/17.9	24.03/15.4/12.8	28.72/13.0/6.43	22.32/18.0/10.3	
	² 32.71/9.93/5.66	29.71/12.57/6.71	34.58/4.46/2.74	35.63/5.62/2.50	39.33/3.35/1.90	33.95/3.49/2.61	
	³ 32.23/10.9/6.36	29.53/13.38/6.99	34.09/4.83/2.97	35.36/5.70/2.58	38.99/3.34/2.00	33.69/3.48/2.66	
	⁴ 32.70/9.93/5.67	29.80/12.45/6.58	34.62/4.46/2.71	35.72/5.57/2.47	39.54/3.27/1.85	34.13/3.45/2.56	
	⁵ 32.27/10.9/6.14	29.69/13.09/6.72	34.13/4.79/2.93	35.49/5.60/2.53	39.28/3.28/1.93	33.93/3.46/2.59	
	⁶ 33.31/8.89/5.11	30.76/11.02/5.67	35.13/4.10/2.37	36.28/5.44/2.33	41.41/3.05/1.40	37.79/2.98/1.57	
	⁷ 33.18/9.18/5.33	30.57/11.80/5.88	34.53/4.73/2.55	36.23/5.50/2.34	41.71/2.99/1.38	37.77/3.10/1.61	
Full-Resolution : $D_{\lambda}^{\times 10^{-1}} \downarrow / D_S^{\times 10^{-1}} \downarrow / QNR \uparrow$	FusionNet	¹ 0.37/0.51/0.914	0.16/0.81/0.904	0.17/0.36/0.947	0.30/0.66/0.906	0.23/0.55/0.924	0.19/0.20/0.962
		² 0.18/0.59/0.925	0.34/1.13/0.857	0.29/0.62/0.912	0.65/1.27/0.818	1.16/2.02/0.712	0.64/1.85/0.765
		³ 0.19/0.61/0.921	0.30/1.04/0.869	0.31/0.60/0.912	0.61/1.24/0.824	1.04/1.94/0.728	0.64/1.91/0.760
		⁴ 0.19/0.58/0.924	0.30/1.05/0.868	0.22/0.57/0.923	0.61/1.23/0.825	0.95/1.84/0.745	0.42/1.60/0.806
		⁵ 0.17/0.58/0.925	0.28/1.03/0.872	0.27/0.60/0.915	0.59/1.22/0.828	0.92/1.84/0.746	0.55/1.82/0.776
		⁶ 0.17/0.64/0.920	0.14/0.86/0.902	0.08/0.39/0.954	0.25/0.86/0.892	0.15/0.62/0.924	0.03/0.09/0.988
		⁷ 0.18/0.64/0.919	0.14/0.84/0.903	0.09/0.37/0.954	0.30/0.85/0.889	0.21/0.61/0.920	0.04/0.18/0.978
	GPPNN	¹ 0.37/0.52/0.913	0.20/ 0.67/0.914	0.09/ 0.27/0.965	0.05/0.18/0.977	0.06/0.18/0.976	0.02/ 0.02/0.997
		² 0.29/0.79/0.895	0.69/1.39/0.802	0.22/0.51/0.928	0.55/1.17/0.835	0.96/1.83/0.745	0.49/1.62/0.799
		³ 0.35/0.78/0.890	0.71/1.42/0.799	0.41/0.55/0.907	0.59/1.18/0.832	1.04/1.90/0.731	0.63/1.81/0.770
		⁴ 0.20/0.73/0.909	0.37/1.14/0.854	0.10/0.41/0.950	0.43/1.09/0.854	0.53/1.42/0.816	0.32/1.10/0.862
		⁵ 0.21/0.69/0.912	0.33/1.18/0.854	0.23/0.48/0.931	0.34/0.97/0.873	0.46/1.43/0.820	0.32/1.41/0.833
		⁶0.11/0.65/0.925	0.19/0.91/0.891	<u>0.06/0.30/0.964</u>	0.28/0.94/0.881	0.18/0.72/0.912	0.06/0.06/0.988
		⁷ 0.15/0.68/0.918	<u>0.19/0.98/0.885</u>	0.07/0.34/0.959	0.32/0.96/0.876	0.16/0.89/0.897	0.01/0.03/0.995
	PreMix	¹ 0.12/ 0.12/0.976	0.60/0.92/0.854	0.31/0.37/0.933	0.60/0.72/0.872	0.32/0.40/0.929	0.03/0.06/0.991
		² 0.23/0.76/0.903	0.42/1.25/0.839	0.14/0.45/0.942	0.53/1.16/0.839	0.78/1.69/0.771	0.38/1.48/0.822
		³ 0.27/0.74/0.901	0.45/1.26/0.835	0.27/0.59/0.915	0.54/1.20/0.834	0.92/1.86/0.745	0.60/1.92/0.762
		⁴ 0.19/0.71/0.911	0.33/1.15/0.856	0.07/0.35/0.958	0.45/1.08/0.854	0.56/1.44/0.812	0.18/1.15/0.870
		⁵ 0.24/0.69/0.909	0.35/1.14/0.855	0.18/0.51/0.932	0.50/1.16/0.841	0.72/1.67/0.778	0.38/1.68/0.802
		⁶ 0.15/0.68/0.918	<u>0.22/1.01/0.880</u>	0.04/0.30/0.966	0.28/0.94/0.881	0.14/0.71/0.916	0.03/0.16/0.981
		⁷ 0.18/0.68/0.916	0.25/1.02/0.876	0.06/0.37/0.957	0.38/1.06/0.861	0.19/0.83/0.900	0.03/0.10/0.987

Continued to next page.

Model	WorldView-2	WorldView-3	WorldView-4	IKONOS	QuickBird	GaoFen-2	
Full-Resolution	PEMAE	¹ 1.00/1.24/0.797	0.64/1.00/0.846	0.89/0.84/0.841	0.56/ <u>0.65</u> /0.883	0.69/ <u>0.33</u> / <u>0.901</u>	0.59/0.24/0.920
		² 0.25/0.68/0.910	0.39/1.13/0.852	0.25/0.59/0.918	0.51/1.08/0.849	0.98/1.76/0.747	0.72/1.86/0.759
		³ 0.35/0.66/0.901	0.52/1.18/0.836	0.32/0.61/0.910	0.77/1.24/0.811	1.19/1.97/0.713	0.73/2.02/0.743
		⁴ <u>0.25</u> /0.67/0.910	0.36/1.11/0.857	0.20/0.56/0.925	0.49/1.06/0.852	0.86/1.70/0.763	0.60/1.78/0.775
		⁵ 0.37/0.66/0.900	0.50/1.15/0.842	0.28/0.59/0.915	0.72/1.23/0.816	1.08/1.91/0.727	0.59/1.91/0.763
		⁶ <u>0.28/0.62/0.913</u>	<u>0.28/0.90/0.885</u>	<u>0.15/0.33/0.952</u>	<u>0.29/0.77/0.897</u>	<u>0.36/0.87/0.881</u>	<u>0.07/0.14/0.980</u>
		⁷ 0.36/ <u>0.59</u> /0.907	0.39/0.98/0.867	0.18/0.49/0.934	0.53/0.89/0.864	0.43/0.99/0.863	0.14/0.29/0.957
	PanMamba	¹ 2.44/2.33/0.580	1.06/1.33/0.779	1.54/1.56/0.720	2.37/1.31/0.667	3.15/1.88/0.565	1.96/1.72/0.671
		² 0.60/0.91/0.855	1.02/1.56/0.759	0.49/0.74/0.882	1.14/1.39/0.765	1.67/2.19/0.656	1.03/2.02/0.720
		³ 0.73/0.97/0.838	0.89/1.40/0.785	0.51/0.69/0.885	1.16/1.34/0.769	1.70/2.17/0.658	1.16/2.26/0.689
		⁴ 0.60/0.91/0.855	0.91/1.47/0.776	0.44/0.71/0.889	1.08/1.35/0.775	1.57/2.12/0.670	0.95/1.98/0.729
		⁵ 0.65/0.92/0.849	0.80/1.34/0.798	0.50/0.71/0.884	1.08/ <u>1.28</u> /0.782	1.60/2.10/0.672	1.08/2.22/0.699
		⁶ <u>0.46/0.82/0.876</u>	0.62/1.29/0.818	<u>0.30/0.59/0.913</u>	0.92/1.35/0.788	0.98/1.75/0.746	<u>0.19/0.77/0.906</u>
		⁷ <u>0.54/0.86/0.865</u>	<u>0.53/1.20/0.834</u>	0.37/0.71/0.896	<u>0.86/1.28/0.800</u>	<u>0.87/1.80/0.750</u>	0.34/1.13/0.857

Table 3: Quantitative comparison on reduced- and full-resolution evaluation. \uparrow : Higher is better, \downarrow : Lower is better. Underlined values indicate the best results among different configurations of one model. **Bold** values indicate the best across all models. Index convention: ¹Training from scratch, ²0-shot generalization (pre-trained on ImageNet), ³0-shot generalization (pre-trained on SkyScript), ⁴1-shot freeze-tuning (pretrained on ImageNet), ⁵1-shot freeze-tuning (pretrained on SkyScript), ⁶1-shot full-tuning (pretrained on ImageNet), ⁷1-shot full-tuning (pretrained on SkyScript).

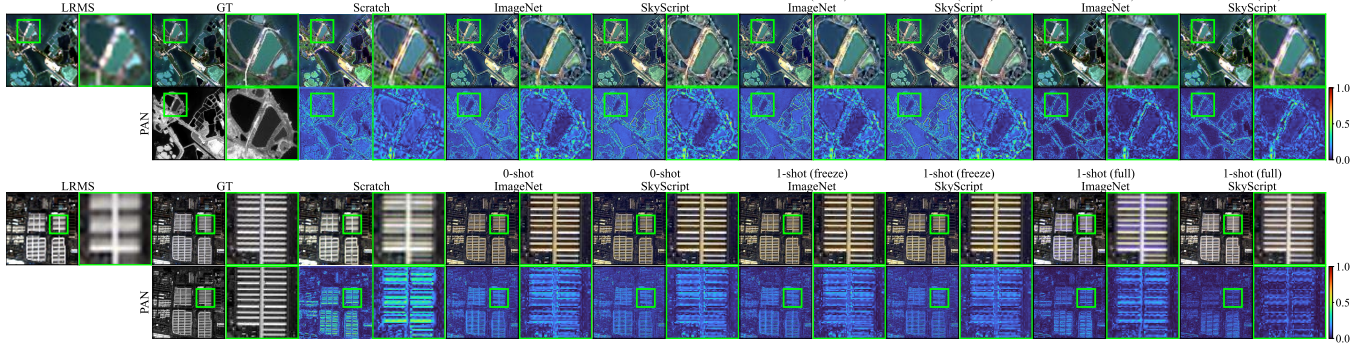


Figure 2: Visualization of predictions and mean absolute errors on IKONOS (upper) and QuickBird (lower) with PEMA (Cui et al. 2024a) model. Bright boxes indicate zoomed-in regions.

preserving spatial structure, resulting in more accurate and visually pleasing fusion outputs. These visualizations further demonstrate that the proposed pretraining and adaptation strategy is effective in both quantitative and qualitative terms, enabling robust cross-domain pansharpening with minimal real data. Fig. 5 in Appendix illustrates the convergence behavior. Zero-shot inference (pretrained only) outperforms models trained from scratch, demonstrating strong generalization. Pretraining followed by fine-tuning leads to much faster and higher convergence compared to training from scratch, highlighting the value of learned spatial-spectral priors. For tuning strategy, full-tuning consistently outperforms freeze-tuning, indicating that full adaptation is crucial for optimal performance. Interestingly, pretraining and fine-tuning on ImageNet yields better results than on SkyScript, likely due to the greater diversity and scale of ImageNet, which helps the model learn more generalizable spatial features, while SkyScript provides more domain-specific but potentially less diverse priors.

Conclusion

In this paper, we proposed pretraining and fine-tuning for pansharpening, leveraging large-scale simulated datasets to learn robust spatial-spectral priors. By pretraining fusion models on natural and remote sensing images and fine-tuning them with extremely limited manner, the models demonstrated significant improvements in generalization performance across different satellite sensors and imaging conditions. Extensive experiments on benchmark datasets showed that the proposed approach enhances the adaptability of models to unseen data with minimal real-world data.

Despite these promising results, while our method improves generalization, it still relies on simulated data, which may not fully capture the complexity of real-world sensor variations. Future research could investigate the incorporation of more diverse datasets, including hyperspectral and synthetic data, to further enhance model robustness. Additionally, exploring more efficient fine-tuning strategies and extending the pretraining paradigm to other remote sensing tasks could lead to more versatile and scalable solutions.

Appendix

Datasets

For pretraining, we utilize two large-scale datasets: ImageNet (Deng et al. 2009) and SkyScript (Wang et al. 2024b). For each dataset, we use 40,000 training images and 10,000 validation images. The images are processed to simulate multispectral and panchromatic data pairs for pansharpening pretraining.

For zero-shot and one-shot evaluation, we employ six satellite datasets (Meng et al. 2021) including WorldView-2, WorldView-3, WorldView-4, IKONOS, QuickBird, and Gaofen-2. Each satellite dataset contains hundreds of image pairs, where we use 10 images for tuning and the remaining images for validation. Training will be conducted following Wald’s protocol (Wald, Ranchin, and Mangolini 1997), and testing will be conducted on both reduced- and full-resolution.

Metrics

For reduced-resolution evaluation, we assess model performance using Peak Signal-to-Noise Ratio (PSNR), Spectral Angle Mapper (SAM), Relative Dimensionless Global Error in Synthesis (ERGAS), Correlation Coefficient (CC), Structural Similarity Index Measure (SSIM), and Mean Absolute Error (MAE). For full-resolution evaluation, we employ Spectral Distortion Index (D_λ), Spatial Distortion Index (D_S), and Quality with No Reference (QNR) (Alparone et al. 2008) to quantitatively measure the quality of the fused images.

Implementation Details

All model implementations are available from the official site. Experiments are conducted using PyTorch 2.1.1 with 4 NVIDIA RTX 4090 GPUs. For pretraining, we employ a batch size of 12 with AdamW (Loshchilov and Hutter 2019) optimizer and a learning rate of 10^{-3} . The training uses linear warmup cosine annealing scheduler for 100 epochs, with warm up for 10 epochs. For fine-tuning, we use one single pair of multispectral and panchromatic images with AdamW (Loshchilov and Hutter 2019) optimizer and a reduced learning rate of 10^{-4} . The fine-tuning employs cosine annealing scheduler for 40 epochs. The best model is selected based on the highest PSNR value on validation set.

Additional Experimental Results

Quantitative Results. Table 4 presents an additional quantitative comparison (SSIM, MAE, and CC metrics) of different models across six satellite datasets under various training configurations, including training from scratch, zero-shot generalization, and one-shot fine-tuning with both ImageNet and SkyScript pretraining. The results demonstrate that our proposed method achieves superior performance in most scenarios, particularly in the one-shot learning settings.

Pretraining Visualization Results. Figs. 3 and 4 demonstrate the effectiveness of our pretraining strategy on ImageNet and SkyScript datasets, respectively. These visualiza-

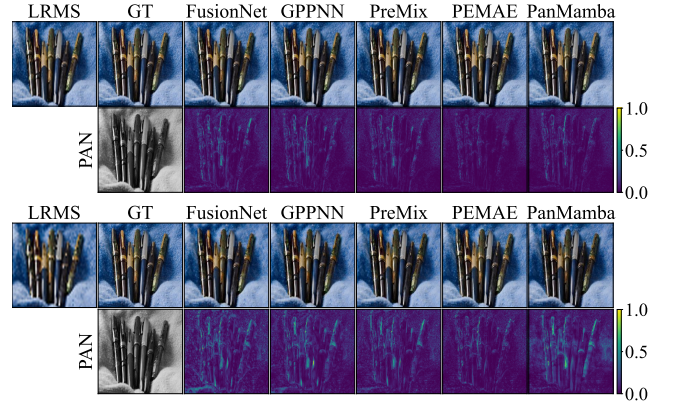


Figure 3: Visualization of simulated MS, PAN, predictions, and error maps on ImageNet (Deng et al. 2009) with $4\times$ (upper) and $8\times$ (lower) spatial resolution degradations.

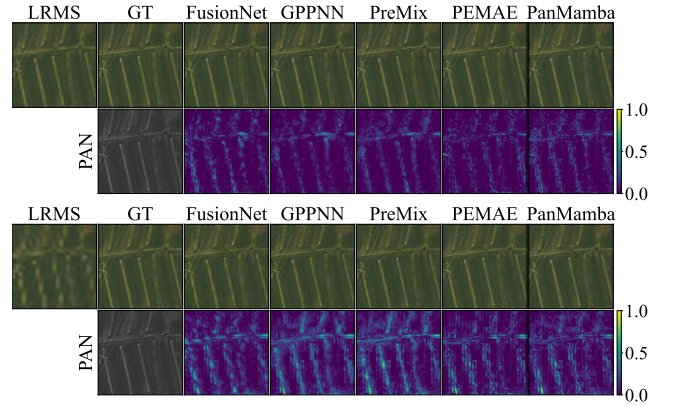


Figure 4: Visualization of simulated MS, PAN, predictions, and error maps on SkyScript (Wang et al. 2024b) with $4\times$ (upper) and $8\times$ (lower) spatial resolution degradations.

tions show the simulated multispectral (MS) and panchromatic (PAN) images, along with the model predictions and corresponding error maps.

Figs. 6 and 7 provide additional visual comparisons of different pansharpening methods on WorldView-4 and WorldView-2 datasets, respectively. The visual results clearly demonstrate the superior performance of pretraining and fine-tuning in preserving both spectral information and spatial details. Our approach shows better edge preservation, reduced artifacts, and more accurate spectral reproduction.

Model	WorldView-2	WorldView-3	WorldView-4	IKONOS	Quickbird	Gaofen-2
FusionNet	¹ 0.793/2.38/0.824	0.859/1.98/0.892	0.913/1.26/0.925	0.888/1.23/0.904	0.958/0.63/0.907	0.928/0.87/0.939
	² 0.847/1.82/0.877	0.827/2.24/0.857	0.891/1.34/0.905	0.879/1.24/0.878	0.909/0.82/0.825	0.786/1.60/0.788
	³ 0.846/1.85/0.875	0.825/2.20/0.861	0.889/1.40/0.902	0.879/1.25/0.878	0.910/0.83/0.824	0.779/1.67/0.778
	⁴ 0.857/1.76/0.885	0.834/2.17/0.864	0.901/1.26/0.914	0.888/1.18/0.886	0.922/0.75/0.841	0.812/1.43/0.819
	⁵ 0.852/1.80/0.880	0.833/2.13/0.867	0.896/1.34/0.908	0.886/1.20/0.885	0.921/0.77/0.837	0.800/1.54/0.800
	⁶ 0.886/1.60/0.905	0.866/1.93/0.898	0.919/1.11/0.933	0.913/1.00/0.919	0.963/0.49/0.924	0.930/0.78/0.945
	⁷ 0.884/1.61/0.906	0.866/1.94/0.902	0.922/1.11/0.941	0.911/1.01/0.919	0.964/0.48/0.924	0.925/0.81/0.943
GPPNN	¹ 0.817/2.18/0.862	0.833/2.14/0.885	0.896/1.26/0.936	0.849/1.29/0.888	0.945/0.55/0.911	0.929/0.77/0.946
	² 0.870/1.73/0.894	0.807/2.40/0.851	0.885/1.40/0.894	0.880/1.23/0.878	0.910/0.80/0.828	0.781/1.62/0.785
	³ 0.864/1.80/0.889	0.810/2.37/0.855	0.875/1.60/0.886	0.879/1.23/0.878	0.910/0.81/0.832	0.779/1.66/0.786
	⁴ 0.879/1.64/0.902	0.834/2.13/0.869	0.905/1.21/0.918	0.893/1.13/0.896	0.938/0.63/0.867	0.850/1.21/0.857
	⁵ 0.879/1.67/0.900	0.843/2.09/0.877	0.903/1.29/0.917	0.902/1.07/0.906	0.944/0.59/0.887	0.847/1.23/0.859
	⁶ 0.885/1.58/0.907	0.847/2.01/0.879	0.919/1.09/0.941	0.906/1.03/0.914	0.951/0.54/0.908	0.927/0.79/0.941
	⁷ 0.887/1.57/0.909	0.857/1.96/0.894	0.920/1.09/0.939	0.908/1.03/0.912	0.962/0.49/0.927	0.928/0.78/0.945
PreMix	¹ 0.762/2.25/0.803	0.818/2.46/0.875	0.885/1.39/0.921	0.853/1.37/0.884	0.944/0.59/0.896	0.930/0.79/0.944
	² 0.886/1.59/0.905	0.848/2.07/0.873	0.908/1.22/0.920	0.895/1.14/0.895	0.921/0.75/0.843	0.815/1.49/0.808
	³ 0.873/1.76/0.892	0.837/2.21/0.867	0.898/1.35/0.907	0.885/1.21/0.883	0.914/0.79/0.830	0.800/1.57/0.795
	⁴ 0.894/1.54/0.909	0.859/1.99/0.882	0.914/1.16/0.926	0.904/1.07/0.903	0.935/0.67/0.861	0.844/1.32/0.845
	⁵ 0.881/1.70/0.898	0.850/2.09/0.877	0.906/1.26/0.917	0.896/1.14/0.893	0.929/0.71/0.848	0.827/1.42/0.824
	⁶ 0.901/1.46/0.919	0.877/1.83/0.906	0.925/1.05/0.942	0.918/0.97/0.923	0.965/0.47/0.931	0.935/0.75/0.947
	⁷ 0.892/1.55/0.911	0.867/1.91/0.898	0.923/1.08/0.939	0.909/1.04/0.912	0.962/0.49/0.928	0.929/0.78/0.945
PEMAE	¹ 0.781/2.48/0.739	0.787/2.58/0.805	0.847/1.83/0.816	0.871/1.30/0.866	0.955/0.58/0.878	0.917/0.93/0.904
	² 0.882/1.60/0.882	0.841/2.06/0.858	0.901/1.25/0.908	0.893/1.14/0.892	0.925/0.73/0.826	0.809/1.49/0.802
	³ 0.875/1.70/0.890	0.830/2.15/0.863	0.892/1.36/0.908	0.885/1.17/0.887	0.917/0.75/0.833	0.797/1.53/0.796
	⁴ 0.886/1.57/0.886	0.849/2.01/0.865	0.907/1.20/0.914	0.899/1.10/0.898	0.932/0.69/0.837	0.824/1.40/0.820
	⁵ 0.879/1.68/0.894	0.842/2.07/0.873	0.900/1.30/0.916	0.894/1.12/0.896	0.928/0.69/0.849	0.817/1.42/0.818
	6 0.903/1.46/0.904	0.878/1.82/0.900	0.922/1.07/0.944	0.922/0.94/0.934	0.968/0.46/0.934	0.930/0.77/0.946
	⁷ 0.894/1.55/0.900	0.865/1.90/0.897	0.924/1.08/0.941	0.918/0.96/0.928	0.967/0.46/0.932	0.929/0.77/0.946
PanMamba	¹ 0.590/6.45/0.549	0.698/4.94/0.809	0.752/7.04/0.837	0.749/5.88/0.794	0.884/3.17/0.584	0.809/6.58/0.762
	² 0.863/1.77/0.885	0.819/2.27/0.851	0.886/1.41/0.894	0.876/1.27/0.877	0.916/0.81/0.820	0.779/1.66/0.774
	³ 0.845/1.97/0.882	0.812/2.35/0.856	0.878/1.57/0.891	0.870/1.31/0.868	0.907/0.84/0.814	0.769/1.72/0.765
	⁴ 0.863/1.77/0.885	0.823/2.24/0.853	0.888/1.40/0.894	0.879/1.25/0.878	0.920/0.78/0.822	0.786/1.63/0.777
	⁵ 0.851/1.95/0.883	0.820/2.29/0.858	0.880/1.56/0.891	0.873/1.29/0.871	0.913/0.81/0.818	0.778/1.67/0.770
	⁶ 0.885/1.62/0.896	0.861/1.96/0.883	0.914/1.21/0.921	0.895/1.16/0.897	0.957/0.58/0.900	0.913/0.98/0.921
	⁷ 0.879/1.71/0.899	0.852/2.04/0.883	0.902/1.40/0.909	0.895/1.16/0.896	0.957/0.56/0.906	0.904/1.03/0.911

Table 4: Quantitative comparison on reduced-resolution evaluation with metrics: SSIM \uparrow / MAE $\times 10^{-2}$ \downarrow / CC \uparrow . \uparrow : Higher is better, \downarrow : Lower is better. Underlined values indicate the best results among different configurations of one model. **Bold** values indicate the best across all models. Index convention: ¹Training from scratch, ²0-shot generalization (pre-trained on ImageNet), ³0-shot generalization (pre-trained on SkyScript), ⁴1-shot freeze-tuning (pretrained on ImageNet), ⁵1-shot freeze-tuning (pretrained on SkyScript), ⁶1-shot full-tuning (pretrained on ImageNet), ⁷1-shot full-tuning (pretrained on SkyScript).

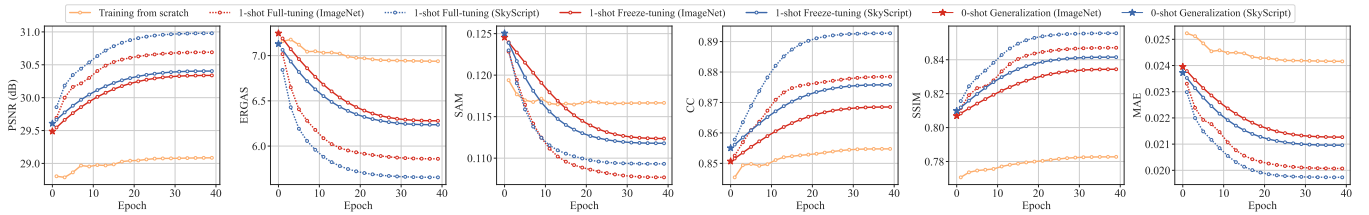
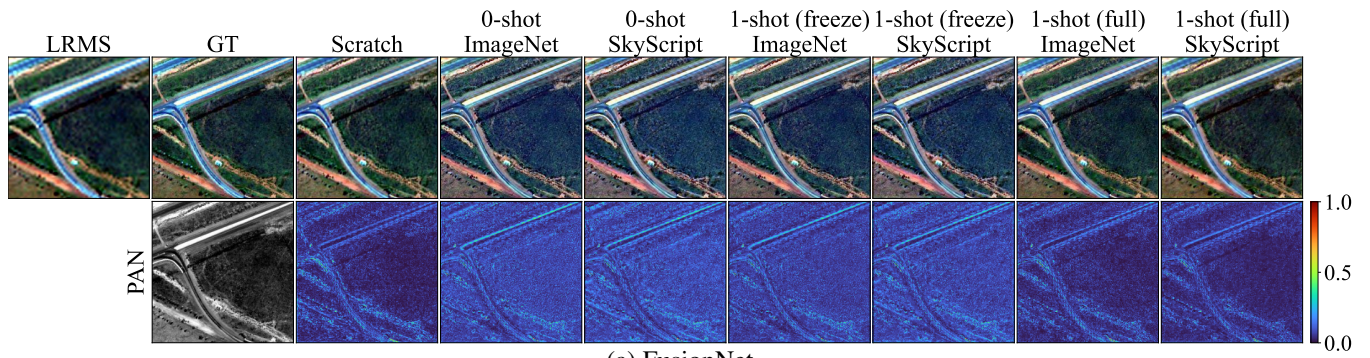
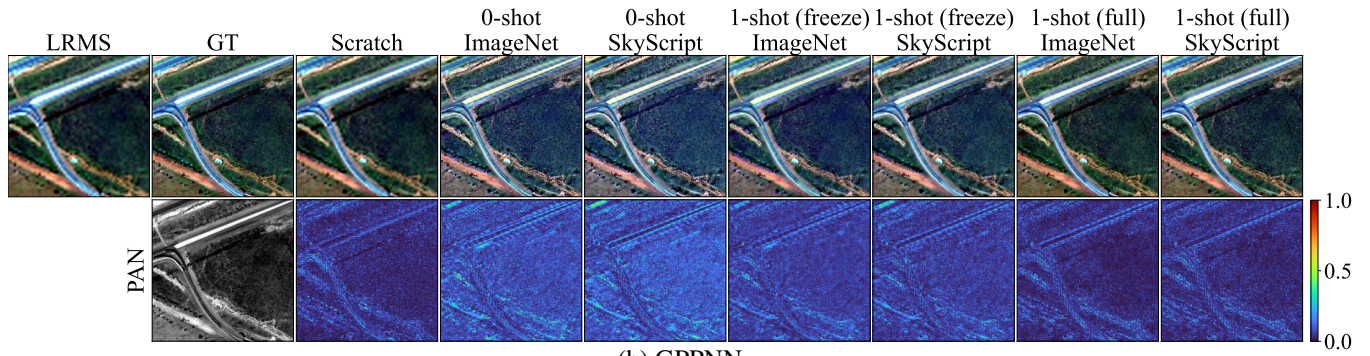


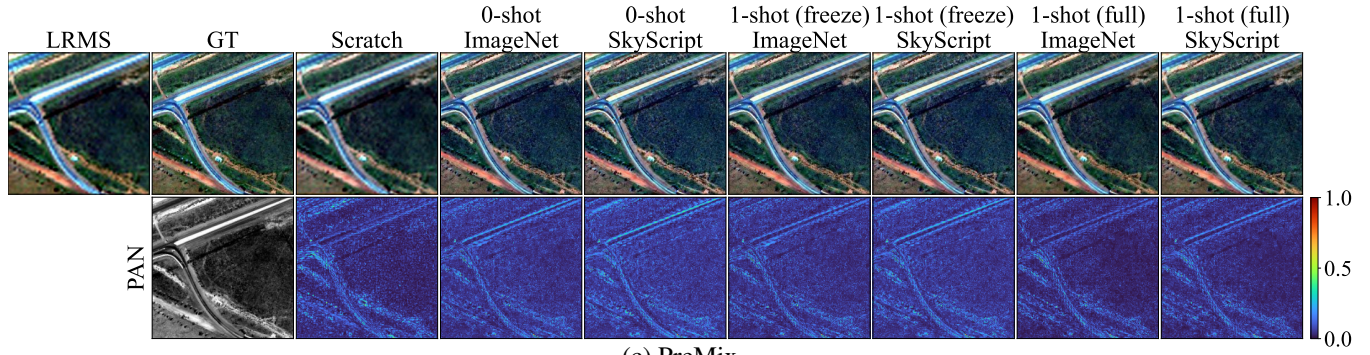
Figure 5: Convergence of GPPNN (Xu et al. 2021) on WorldView-3 (averaged results on all training images).



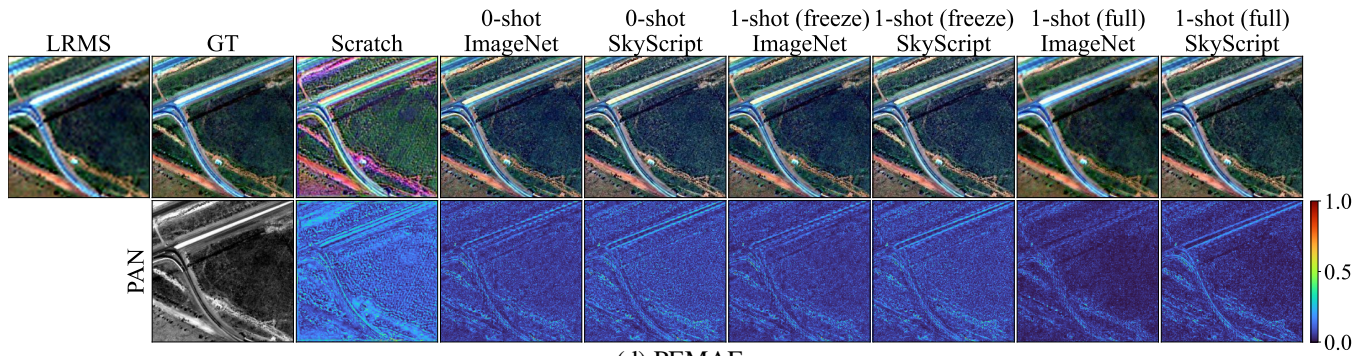
(a) FusionNet



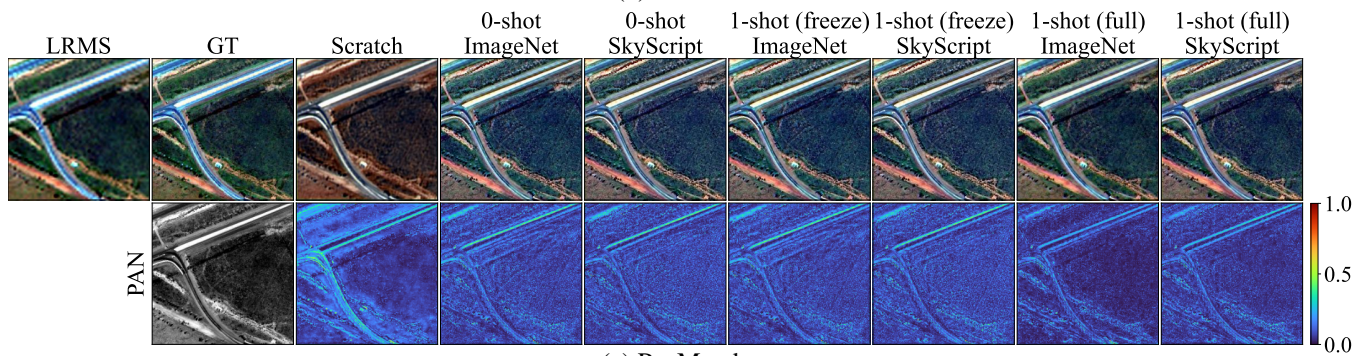
(b) GPPNN



(c) PreMix



(d) PEMAE



(e) PanMamba

Figure 6: Visual comparison of different models on WorldView-4.

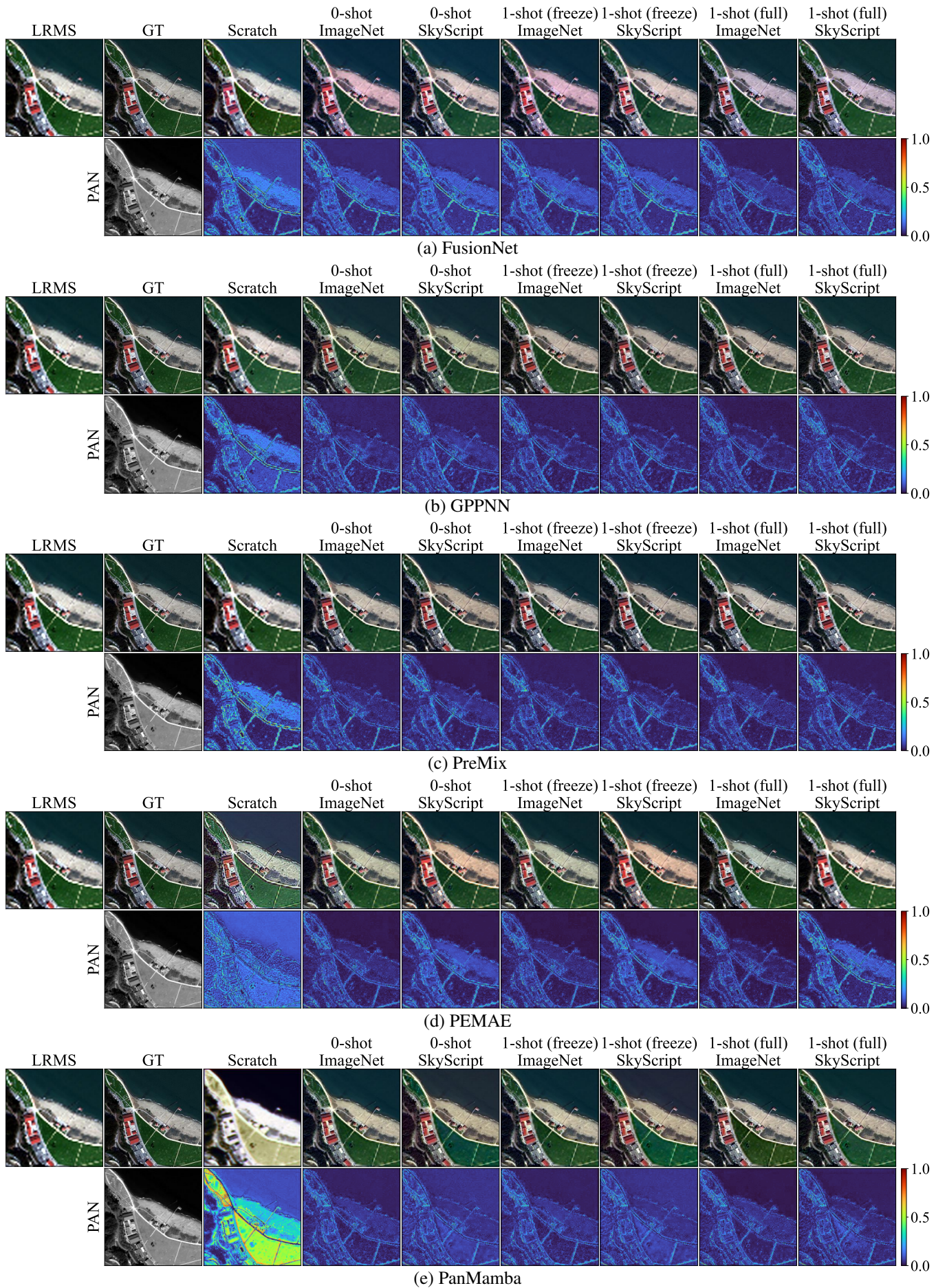


Figure 7: Visual comparison of different models on WorldView-2.

References

- Aiazzi, B.; Alparone, L.; Baronti, S.; and Garzelli, A. 2002. Context-driven fusion of high spatial and spectral resolution images based on oversampled multiresolution analysis. *IEEE Transactions on Geoscience and Remote Sensing*, 40(10): 2300–2312.
- Aiazzi, B.; Alparone, L.; Baronti, S.; Garzelli, A.; and Selva, M. 2006. MTF-tailored Multiscale Fusion of High-resolution MS and Pan Imagery. *Photogrammetric Engineering and Remote Sensing*, 72: 591–596.
- Alparone, L.; Aiazzi, B.; Baronti, S.; Garzelli, A.; Nencini, F.; and Selva, M. 2008. Multispectral and panchromatic data fusion assessment without reference. *Photogrammetric Engineering and Remote Sensing*, 74(2): 193–200.
- Bandara, W. G. C.; and Patel, V. M. 2022. Hypertransformer: A textural and spectral feature fusion Transformer for pansharpening. In *IEEE Conference on Computer Vision and Pattern Recognition*, 1767–1777.
- Cao, Z.; Cao, S.; Deng, L.-J.; Wu, X.; Hou, J.; and Vivone, G. 2024. Diffusion model with disentangled modulations for sharpening multispectral and hyperspectral images. *Information Fusion*, 104: 102158.
- Ciotola, M.; Poggi, G.; and Scarpa, G. 2023. Unsupervised Deep Learning-Based Pansharpening With Jointly Enhanced Spectral and Spatial Fidelity. *IEEE Transactions on Geoscience and Remote Sensing*, 61: 1–17.
- Cui, Y.; Liu, P.; Ma, Y.; Chen, L.; Xu, M.; and Guo, X. 2024a. Pixel-Wise Ensembled Masked Autoencoder for Multispectral Pansharpening. *IEEE Transactions on Geoscience and Remote Sensing*, 62: 1–22.
- Cui, Y.; Liu, P.; Ma, Y.; Chen, L.; Xu, M.; and Guo, X. 2025a. Pansharpening via predictive filtering with element-wise feature mixing. *ISPRS Journal of Photogrammetry and Remote Sensing*, 219: 22–37.
- Cui, Y.; Liu, P.; Song, B.; Zhao, L.; Ma, Y.; and Chen, L. 2024b. Reconstruction of Large-Scale Missing Data in Remote Sensing Images Using Extend-GAN. *IEEE Geoscience and Remote Sensing Letters*, 21: 1–5.
- Cui, Y.; Liu, P.; and Zhang, H. 2025. Empowering Your Pansharpening Models with Generalizability: Unified Distribution is All You Need. In *Proceedings of the IEEE/CVF International Conference on Computer Vision (ICCV)*, 11850–11860.
- Cui, Y.; Zhang, J.; Liu, P.; Song, W.; and Zeng, Y. 2025b. Overcoming the Identity Mapping Problem in Self-Supervised Hyperspectral Anomaly Detection. *arXiv:2504.04115*.
- Dao, T.; and Gu, A. 2024. Transformers are SSMs: Generalized Models and Efficient Algorithms Through Structured State Space Duality. In *International Conference on Machine Learning (ICML)*.
- Deng, J.; Dong, W.; Socher, R.; Li, L.-J.; Li, K.; and Fei-Fei, L. 2009. ImageNet: A large-scale hierarchical image database. In *IEEE Conference on Computer Vision and Pattern Recognition*, 248–255.
- Deng, L.-J.; Vivone, G.; Jin, C.; and Chanussot, J. 2021. Detail Injection-Based Deep Convolutional Neural Networks for Pansharpening. *IEEE Transactions on Geoscience and Remote Sensing*, 59(8): 6995–7010.
- Deng, L.-j.; Vivone, G.; Paoletti, M. E.; Scarpa, G.; He, J.; Zhang, Y.; Chanussot, J.; and Plaza, A. 2022. Machine Learning in Pansharpening: A benchmark, from shallow to deep networks. *IEEE Geoscience and Remote Sensing Magazine*, 10(3): 279–315.
- Deng, S.; Deng, L.-J.; Wu, X.; Ran, R.; and Wen, R. 2023. Bidirectional dilation Transformer for multispectral and hyperspectral image fusion. In *International Joint Conference on Artificial Intelligence*. ISBN 978-1-956792-03-4.
- Dian, R.; Guo, A.; and Li, S. 2023. Zero-Shot Hyperspectral Sharpening. *IEEE Transactions on Pattern Analysis and Machine Intelligence*, 45(10): 12650–12666.
- Dosovitskiy, A.; Beyer, L.; Kolesnikov, A.; Weissenborn, D.; Zhai, X.; Unterthiner, T.; Dehghani, M.; Minderer, M.; Heigold, G.; Gelly, S.; Uszkoreit, J.; and Houlsby, N. 2021. An Image is Worth 16x16 Words: Transformers for Image Recognition at Scale. *International Conference on Learning Representations*.
- Gu, A.; and Dao, T. 2023. Mamba: Linear-Time Sequence Modeling with Selective State Spaces. *arXiv preprint arXiv:2312.00752*.
- He, X.; Cao, K.; Zhang, J.; Yan, K.; Wang, Y.; Li, R.; Xie, C.; Hong, D.; and Zhou, M. 2025. Pan-Mamba: Effective pan-sharpening with state space model. *Information Fusion*, 115: 102779.
- Jiang, H.; and Chen, Z. 2025. Hyperspectral Pansharpening with Transformer-Based Spectral Diffusion Priors. In *2025 IEEE/CVF Winter Conference on Applications of Computer Vision Workshops (WACVW)*, 544–553.
- Krizhevsky, A.; Sutskever, I.; and Hinton, G. E. 2017. ImageNet classification with deep convolutional neural networks. *Commun. ACM*, 60(6): 84–90.
- Laben, C. A.; and Brower, B. V. 2000. Process for enhancing the spatial resolution of multispectral imagery using pansharpening. US Patent 6,011,875.
- Liu, P.; Li, J.; Wang, L.; and He, G. 2022. Remote Sensing Data Fusion With Generative Adversarial Networks: State-of-the-art methods and future research directions. *IEEE Geoscience and Remote Sensing Magazine*, 10(2): 295–328.
- Liu, P.; Wang, L.; Chen, J.; and Cui, Y. 2024. Semiblind Compressed Sensing: A Bidirectional-Driven Method for Spatiotemporal Fusion of Remote Sensing Images. *IEEE Journal of Selected Topics in Applied Earth Observations and Remote Sensing*, 17: 19048–19066.
- Liu, Q.; Zhou, H.; Xu, Q.; Liu, X.; and Wang, Y. 2020. PS-GAN: A generative adversarial network for remote sensing image pan-sharpening. *IEEE Transactions on Geoscience and Remote Sensing*, 59(12): 10227–10242.
- Liu, X.; Liu, X.; Dai, H.; Kang, X.; Plaza, A.; and Zu, W. 2023. Mun-GAN: a multiscale unsupervised network for remote sensing image pansharpening. *IEEE Transactions on Geoscience and Remote Sensing*, 61: 1–18.

- Loshchilov, I.; and Hutter, F. 2019. Decoupled Weight Decay Regularization. In *International Conference on Learning Representations*.
- Ma, J.; Yu, W.; Chen, C.; Liang, P.; Guo, X.; and Jiang, J. 2020. Pan-GAN: An unsupervised pan-sharpening method for remote sensing image fusion. *Information Fusion*, 62: 110–120.
- Masi, G.; Cozzolino, D.; Verdoliva, L.; and Scarpa, G. 2016. Pansharpening by Convolutional Neural Networks. In *Remote Sensing*, volume 8, 594.
- Meng, Q.; Shi, W.; Li, S.; and Zhang, L. 2023. PanDiff: A novel pansharpening method based on denoising diffusion probabilistic model. *IEEE Transactions on Geoscience and Remote Sensing*, 61: 1–17.
- Meng, X.; Wang, N.; Shao, F.; and Li, S. 2022. Vision Transformer for pansharpening. *IEEE Transactions on Geoscience and Remote Sensing*, 60: 1–11.
- Meng, X.; Xiong, Y.; Shao, F.; Shen, H.; Sun, W.; Yang, G.; Yuan, Q.; Fu, R.; and Zhang, H. 2021. A Large-Scale Benchmark Data Set for Evaluating Pansharpening Performance: Overview and Implementation. *IEEE Geoscience and Remote Sensing Magazine*, 9(1): 18–52.
- Peng, S.; Zhu, X.; Deng, H.; Deng, L.-J.; and Lei, Z. 2024. FusionMamba: Efficient remote sensing image fusion with state space model. *IEEE Transactions on Geoscience and Remote Sensing*.
- Rahmani, S.; Strait, M.; Merkurjev, D.; Moeller, M.; and Wittman, T. 2010. An Adaptive IHS Pan-Sharpener Method. *IEEE Geoscience and Remote Sensing Letters*, 7(4): 746–750.
- Rui, X.; Cao, X.; Pang, L.; Zhu, Z.; Yue, Z.; and Meng, D. 2024. Unsupervised hyperspectral pansharpening via low-rank diffusion model. *Information Fusion*, 107: 102325.
- Shah, V. P.; Younan, N. H.; and King, R. L. 2008. An Efficient Pan-Sharpener Method via a Combined Adaptive PCA Approach and Contourlets. *IEEE Transactions on Geoscience and Remote Sensing*, 46(5): 1323–1335.
- Sun, E.; Cui, Y.; Liu, P.; and Yan, J. 2026. A decade of deep learning for remote sensing spatiotemporal fusion: Advances, challenges, and opportunities. *Information Fusion*, 126: 103675.
- Vaswani, A.; Shazeer, N.; Parmar, N.; Uszkoreit, J.; Jones, L.; Gomez, A. N.; Kaiser, L. u.; and Polosukhin, I. 2017. Attention is All you Need. In *Advances in Neural Information Processing Systems*, volume 30.
- Vivone, G.; Dalla Mura, M.; Garzelli, A.; Restaino, R.; Scarpa, G.; Ulfarsson, M. O.; Alparone, L.; and Chanussot, J. 2021. A New Benchmark Based on Recent Advances in Multispectral Pansharpening: Revisiting Pansharpening With Classical and Emerging Pansharpening Methods. *IEEE Geoscience and Remote Sensing Magazine*, 9(1): 53–81.
- Vivone, G.; Simões, M.; Dalla Mura, M.; Restaino, R.; Bioucas-Dias, J. M.; Licciardi, G. A.; and Chanussot, J. 2015. Pansharpening Based on Semiblind Deconvolution. *IEEE Transactions on Geoscience and Remote Sensing*, 53(4): 1997–2010.
- Wald, L.; Ranchin, T.; and Mangolini, M. 1997. Fusion of satellite images of different spatial resolutions: Assessing the quality of resulting images. *Photogrammetric Engineering and Remote Sensing*, 63: 691–699.
- Wang, H.; Zhang, H.; Tian, X.; and Ma, J. 2024a. Zero-Sharpen: A universal pansharpening method across satellites for reducing scale-variance gap via zero-shot variation. *Information Fusion*, 101: 102003.
- Wang, Z.; Prabha, R.; Huang, T.; Wu, J.; and Rajagopal, R. 2024b. SkyScript: A Large and Semantically Diverse Vision-Language Dataset for Remote Sensing. *Proceedings of the AAAI Conference on Artificial Intelligence*, 38(6): 5805–5813.
- Wu, Z.-C.; Huang, T.-Z.; Deng, L.-J.; Hu, J.-F.; and Vivone, G. 2022. VO+Net: An Adaptive Approach Using Variational Optimization and Deep Learning for Panchromatic Sharpening. *IEEE Transactions on Geoscience and Remote Sensing*, 60: 1–16.
- Xing, Y.; Qu, L.; Zhang, S.; Feng, J.; Zhang, X.; and Zhang, Y. 2024a. Empower generalizability for pansharpening through text-modulated diffusion model. *IEEE Transactions on Geoscience and Remote Sensing*.
- Xing, Y.; Qu, L.; Zhang, S.; Xu, D.; Yang, Y.; and Zhang, Y. 2025. Dual-Granularity Semantic Guided Sparse Routing Diffusion Model for General Pansharpening. In *Proceedings of the IEEE/CVF Conference on Computer Vision and Pattern Recognition (CVPR)*, 12658–12668.
- Xing, Y.; Qu, L.; Zhang, S.; Zhang, K.; Zhang, Y.; and Bruzzone, L. 2024b. CrossDiff: Exploring self-supervised representation of pansharpening via cross-predictive diffusion model. *IEEE Transactions on Image Processing*.
- Xu, S.; Zhang, J.; Zhao, Z.; Sun, K.; Liu, J.; and Zhang, C. 2021. Deep Gradient Projection Networks for Pansharpening. In *IEEE Conference on Computer Vision and Pattern Recognition*, 1366–1375.
- Yang, J.; Fu, X.-Y.; Hu, Y.; Huang, Y.; Ding, X.; and Paisley, J. 2017. PanNet: A Deep Network Architecture for Pan-Sharpener. *International Conference on Computer Vision*, 1753–1761.
- Yuan, Q.; Wei, Y.; Meng, X.; Shen, H.; and Zhang, L. 2018. A Multiscale and Multidepth Convolutional Neural Network for Remote Sensing Imagery Pan-Sharpener. *IEEE Journal of Selected Topics in Applied Earth Observations and Remote Sensing*, 11(3): 978–989.
- Zhang, Y.; Song, Y.; Duan, Q.; Yu, N.; Li, B.; and Gao, X. 2025. S2CMamba: A Mamba-Based Pansharpening Model Incorporating Spatial and Spectral Consistency. *IEEE Transactions on Geoscience and Remote Sensing*, 63: 1–13.
- Zhong, Y.; Wu, X.; Deng, L.-J.; Cao, Z.; and Dou, H.-X. 2024. SSDiff: Spatial-spectral Integrated Diffusion Model for Remote Sensing Pansharpening. In Globerson, A.; Mackey, L.; Belgrave, D.; Fan, A.; Paquet, U.; Tomczak, J.; and Zhang, C., eds., *Advances in Neural Information Processing Systems*, volume 37, 77962–77986. Curran Associates, Inc.